Diffusion and nucleation in multilayer growth of PTCDI-C_8 studied with in situ X-ray growth oscillations and real-time small angle X-ray scattering

Anton Zykov, Sebastian Bommel, Christopher Wolf, Linus Pithan, Christopher Weber, Paul Beyer, Gonzalo Santoro, Jürgen P. Rabe, and Stefan Kowarik

Citation: The Journal of Chemical Physics **146**, 052803 (2017);
View online: https://doi.org/10.1063/1.4961460
View Table of Contents: http://aip.scitation.org/toc/jcp/146/5
Published by the American Institute of Physics

THE JOURNAL OF CHEMICAL PHYSICS **146**, 052803 (2017)

Diffusion and nucleation in multilayer growth of PTCDI-C_8 studied with *in situ* X-ray growth oscillations and real-time small angle X-ray scattering

Anton Zykov,[1] Sebastian Bommel,[1,2] Christopher Wolf,[1] Linus Pithan,[1] Christopher Weber,[1]
Paul Beyer,[1] Gonzalo Santoro,[2,3] Jürgen P. Rabe,[1,4] and Stefan Kowarik[1,a)]
[1]*Institut für Physik, Humboldt-Universität zu Berlin, Newtonstr. 15, 12489 Berlin, Germany*
[2]*Deutsches Elektronen-Synchrotron (DESY), Notkestr. 85, 22607 Hamburg, Germany*
[3]*Instituto de Ciencia de Materiales de Madrid (ICMM-CSIC), c/Sor Juana Inés de la Cruz 3, 28049 Madrid, Spain*
[4]*IRIS Adlershof, Humboldt-Universität zu Berlin, Zum Großen Windkanal 6, 12489 Berlin, Germany*

(Received 3 May 2016; accepted 30 July 2016; published online 8 September 2016)

We study nucleation and multilayer growth of the perylene derivative PTCDI-C_8 and find a persistent layer-by-layer growth, transformation of island shapes, and an enhancement of molecular diffusivity in upper monolayers (MLs). These findings result from the evaluation of the ML-dependent island densities, obtained by *in situ* real-time grazing incidence small angle X-ray scattering measurements and simultaneous X-ray growth oscillations. Complementary *ex situ* atomic force microscopy snapshots of different growth stages agree quantitatively with both X-ray techniques. The rate and temperature-dependent island density is analyzed using different mean-field nucleation models. Both a diffusion limited aggregation and an attachment limited aggregation model yield in the first two MLs the same critical nucleus size i, similar surface diffusion attempt frequencies in the 10^{19}-10^{20} s^{-1} range, and a decrease of the diffusion barrier E_d in the 2nd ML by 140 meV. *Published by AIP Publishing.* [http://dx.doi.org/10.1063/1.4961460]

I. INTRODUCTION

In the last two decades numerous devices based on small organic molecules have been fabricated, such as organic light emitting devices (OLEDs),[1,2] organic field-effect transistors (OFETs),[3] and organic solar cells.[4,5] It turns out that functionality and thin-film structure are closely related. Thus, a further optimization of (opto-)electronic properties like charge carrier mobilities requires a fundamental understanding of the processes of molecular thin-film growth and structure formation.

As the self-assembly of molecules into functional thin-films is a complex, non-equilibrium phenomenon, for a fundamental understanding numerous simultaneous processes such as adsorption, diffusion, binding, and desorption have to be taken into account. The final film morphology is thus a product of thermodynamics and kinetics, which are influenced by the temperature and the admolecule density. Hence, the most straightforward way to control organic growth is by varying the substrate temperature (T) and the rate of incoming molecules, i.e., the growth rate (GR). T and GR primarily impact the island density N and, therefore, the size of crystalline domains, which, e.g., influences the electron transport in the organic film. Further, evaluating N in the framework of nucleation theory permits to quantify nanoscale processes governing the growth. The dependency of the island density on T and GR is described *via* the nucleation energy E_{nuc} and a scaling exponent p, as reviewed, e.g., by Venables,[6] Brune,[7] and Evans *et al.*[8] While E_{nuc} carries information about, e.g., the energetic barrier for diffusion, from the scaling exponent p one can learn about the number of molecules contained in the largest unstable molecular cluster, i.e., the critical nucleus size i.

Over the last years modern X-ray scattering experiments have proven to be a powerful tool for studying organic thin-film growth and specifically island densities. It has been shown that the temporal evolution of island densities can even be examined *in situ* during the film growth by applying grazing-incidence small-angle X-ray scattering (GISAXS).[9–13] In addition, the evolution of the out-of-plane structure can be simultaneously monitored by specular X-ray reflectivity (XRR) during the growth of thin-films. In numerous studies, non-invasive *in situ* and real-time XRR has been successfully used for analyzing the growth of organic systems.[14–19]

Here, we apply a synchrotron-based *in situ* real-time XRR-GISAXS method in combination with *ex situ* atomic force microscopy (AFM) to investigate the growth of the organic semiconductor N,N'-dioctyl-3,4,9,10-perylene tetracarboxylic diimide (PTCDI-C_8) on silicon oxide. The molecule is known to grow in a highly crystalline fashion and shows an electron mobility of up to 1.7 cm^2/V s.[20,21] It has already been implemented in OFETs and organic solar cells.[22–25] However, aside from a recent publication on the growth of pentacene/PTCDI-C_8 bilayer systems,[26] little is known about the decisive initial stages of PTCDI-C_8 nucleation and growth in the first few MLs.

[a)] Author to whom correspondence should be addressed. Electronic mail: stefan.kowarik@physik.hu-berlin.de

In the present study, we evaluate the in- and out-of-plane morphology of the first PTCDI-C_8 monolayers (MLs). We find significant differences in the growth of the 1st and 2nd ML, including an increased molecular adsorption probability and a transition of the island shapes from roundish in the 1st ML to rectangular in the 2nd ML. Furthermore we observe a lower island density in the 2nd ML, which points towards an enhanced in-plane diffusion of the molecules. To probe this, we first evaluate the evolution of the maximum island density N_{max} as a function of the substrate temperature T and the growth rate GR and make use of mean-field nucleation theory to fit the scaling of N_{max}. We apply not only the frequently used diffusion limited aggregation (DLA) model but also the attachment limited aggregation (ALA) model, as recently established for organic molecular growth.[27] We find the same critical nucleus size i in both MLs, but a 70 meV lower nucleation energy E_{nuc} in the 2nd ML. From the fits we also evaluate the attempt frequencies for surface diffusion ν_0, which are in the order of $10^{19} - 10^{20}\ \mathrm{s}^{-1}$ and therefore larger than for atomic systems. Combining these results, we finally unravel a 140 meV decrease of E_d and correspondingly an increase in the molecular diffusivity in the 2nd ML, which explains the decreased island density. Examining further differences in the nucleation of the 1st and 2nd ML, we discuss potential differences of the molecular thermalization in different MLs by applying the hot-precursor model of nucleation theory.[28]

II. EXPERIMENTAL DETAILS

N,N'-dioctyl-3,4,9,10-perylene tetracarboxylic diimide ($C_{40}H_{42}N_2O_4$, PTCDI-C_8), Fig. 1(a), was purchased from Sigma Aldrich (purity >98.5%). The PTCDI-C_8 molecules were deposited *via* organic molecular beam deposition (OMBD) in a vacuum chamber at a base pressure of $\leq 3.0 \cdot 10^{-7}$ mbar on silicon wafers covered with a native oxide layer at substrate temperatures of 30-100 °C and growth rates of 0.01, 0.1, and 1 nm/min. The growth rate was monitored by a quartz crystal microbalance placed next to the sample holder.

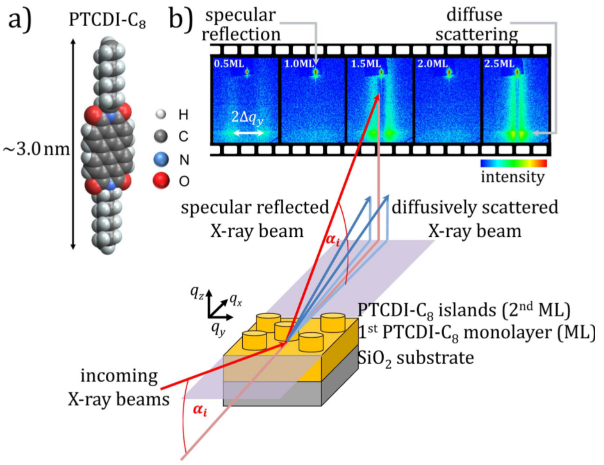

FIG. 1. (a) Sketch of the PTDCDI-C_8 molecule. (b) Scattering geometry during the growth of PTCDI-C_8 on silicon oxide. The simultaneous measurement of the specular reflected and diffusively scattered signals is performed as a function of time.

The substrates were cleaned in a four-step process: during the first three steps, the as-received wafer was cleaned for 10 min in acetone, 2-propanol, and distilled water at room temperature in an ultrasonic bath. As the last step, the substrates were heated in the vacuum chamber to temperatures above 400 °C to remove residuals of organic contaminations.

The X-ray scattering experiments were performed at the MiNaXS P03 beamline of PETRAIII[29,30] at the DESY synchrotron in Hamburg, Germany at a wavelength of $\lambda = 0.0957$ nm. The intensities of the specular reflection and of the diffuse X-ray scattering (in grazing incidence small-angle X-ray scattering (GISAXS) geometry) were monitored simultaneously on a Dectris PILATUS 300 K detector *in situ* and in real-time during the thin-film growth as schematically shown in Fig. 1(b). During all growth experiments the angle of incidence was kept fixed at $\alpha_i = 0.67°$ which equals an out-of-plane scattering vector $q_z = 4\pi/\lambda \cdot \sin(\alpha_i) = 1.54\ \mathrm{nm}^{-1}$. This value corresponds to the so-called anti-Bragg point of the (001) PTCDI-C_8 Bragg reflection $q_z = 1/2 \cdot q_{Bragg}$. To avoid beam damage we linearly translated the sample perpendicular to the incident beam during the real-time growth. The AFM images were recorded on a Bruker MultiMode 8 in ScanAsyst PeakForce tapping mode. For the acquisition we used 2 N/m tips (Olympus).

III. RESULTS

A. *Ex situ* morphology of PTCDI-C_8 films

In Fig. 2 characteristic AFM images of PTCDI-C_8 films are shown as a function of substrate temperature and film thickness (growth rate 0.1 nm/min). The molecules assemble in a nearly upright standing fashion and form islands of about 1 ML height. For higher substrate temperatures and film thicknesses, we find a decreasing island density. In thicker films, simultaneous growth of more than one layer is observed, indicating a slow transition from a layer-by-layer (LBL)

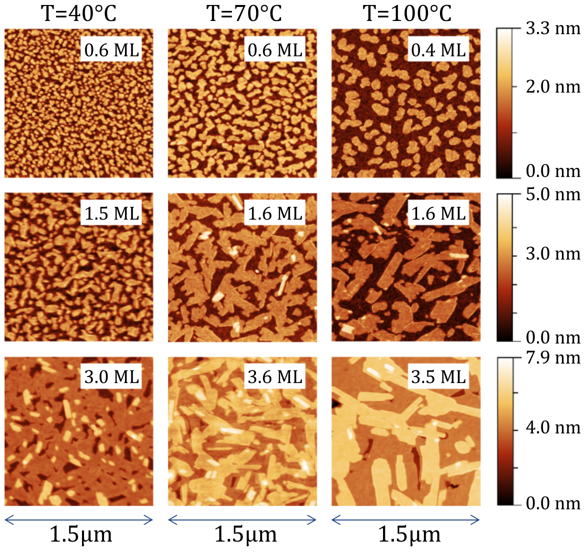

FIG. 2. *Ex situ* AFM snapshots ($1.5 \times 1.5\ \mu m^2$) of 0.5–3.6 ML thick PTCDI-C_8 films grown at three different temperatures. A decrease in the island densities for higher substrate temperatures is visible.

growth towards a rougher 3d growth mode with increasing thickness. Further, islands in the 1st ML have a roundish shape, which changes in the 2nd and higher MLs towards anisotropic, elongated, rod like islands with almost rectangular edges. The form of these islands is comparable to earlier studies[21] of several ML thick PTCDI-C_8 and is also similar to PTCDI-C_{13} islands.[31] Anisotropic island shapes indicate the existence of preferential growth directions due to different surface energies of the crystal facets as well as different growth speeds of different facets.[32]

B. *In situ* temporal evolution of the out-of-plane morphology of PTCDI-C_8 films

While AFM yields real space information about the thin-film morphology, it is usually not feasible to obtain *in situ* and real-time information during the growth, e.g., due to tip shadowing effects. In contrast, it is possible to follow thin-film growth in real-time with X-ray scattering experiments. Our setup, see Fig. 1(b), allows us to simultaneously collect information about the evolution of the in- and out-of-plane morphology.

To monitor the evolution of the out-of-plane morphology of the growing PTCDI-C_8 film we applied *in situ* real-time X-ray reflectivity (XRR) measurements at the anti-Bragg point of the PTCDI-C_8 (001) crystal plane ($q_{anti\text{-}Bragg} = 1/2 \cdot q_{Bragg}$). With increasing molecular exposure (exposure time · growth rate), we observe characteristic growth oscillations of the XRR intensity with a period of two MLs. These originate from alternating constructive and destructive interferences of the X-ray reflections from the individual PTCDI-C_8 MLs.[18] As displayed in Figs. 3(a)-3(c) PTCDI-C_8 exhibits growth-oscillations for several MLs. Such persistently smooth growth has been also observed for the similar PTCDI-C_{13} molecule.[31] The damping of the oscillations depends on the film roughness and hence indicates a slow transition from a smooth layer-by-layer (LBL) growth towards a rougher 3d growth-mode with increasing film thickness, which is in agreement with our observations from the AFM snapshots. This transition proceeds slower than for other organic molecules like pentacene,[15] diindenoperylene,[18] or *para*-sexiphenyl.[33]

We fit the growth oscillations using the software Trofit 0.7.9,[34] which is based on a model by Trofimov and Mokerov[35] and Woll *et al.*[36] and has been applied previously in Refs. 12, 33, and 34. The fits allow us to quantify the height and effective growth rate of the individual MLs and thus the time evolution of the film roughness. The continuous lines in Figs. 3(a)-3(c) show the good agreement of the fits with the data, and the calculated roughness evolution is plotted in Fig. 3(d). The roughness oscillates between low values for completely closed layers and high values for half-filled layers. Further, the roughness continuously increases due to the slow transition from the LBL growth to a 3d growth mode. The half-filled squares in Fig. 3(d) correspond to roughnesses obtained directly from the AFM images. We observe a good agreement with the values from the anti-Bragg fits.

From the anti-Bragg fits we determined also the layer thickness and effective growth rates of the individual MLs. Independent of the substrate temperature and growth rate, a layer thickness of about 2.0 nm was determined for each ML corresponding to almost upright standing molecules. Concerning the effective growth rate, we find that the 1st ML growth proceeds on average 1.4 times slower than the growth of the 2nd and the subsequent MLs. This finding can also be directly deduced from Figs. 3(a)-3(d), where it is clearly visible that it takes less exposure time to accomplish the 2nd ML than the 1st. A slower growing 1st ML was also observed in a study of the similar PTCDI-C_{13} molecule on diverse substrates,[31] where it was attributed to a coverage-dependent adsorption probability of the molecules.

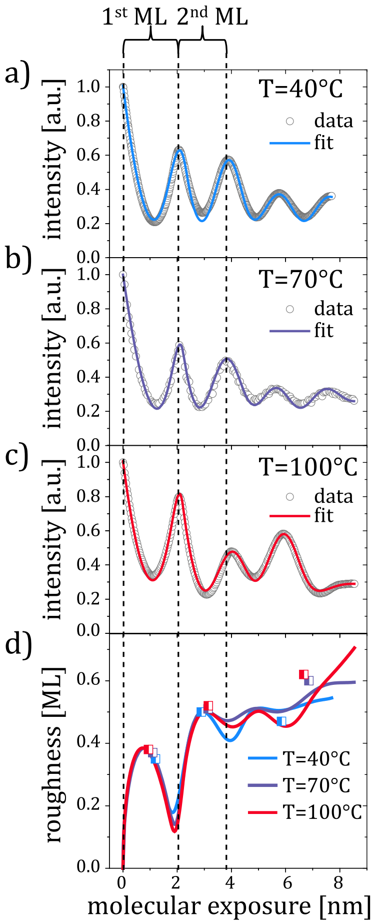

FIG. 3. (a)-(c) Oscillations of the intensity of the specular reflected X-ray beam at the anti-Bragg point acquired *in situ* during the PTCDI-C_8 growth contain information about the time-evolution (molecular exposure = exposure time · growth rate) of the out-of-plane film morphology. The damping of the oscillations is a measure of film roughening indicating a growth-mode transition from layer-by-layer to a rough 3d growth. The lines show the best fits of the anti-Bragg oscillations using a rate equation model. (d) Evolution of the surface roughness as calculated from the model (continuous lines) and from the AFM images (half-filled squares).

C. *In situ* temporal evolution of the in-plane morphology of PTCDI-C_8 films

In addition to the out-of-plane information from the anti-Bragg oscillations, we simultaneously monitored the time evolution of the GISAXS scattering to determine the time evolution of the island density N. In Fig. 4(a), we show the signal on the X-ray detector as measured for a

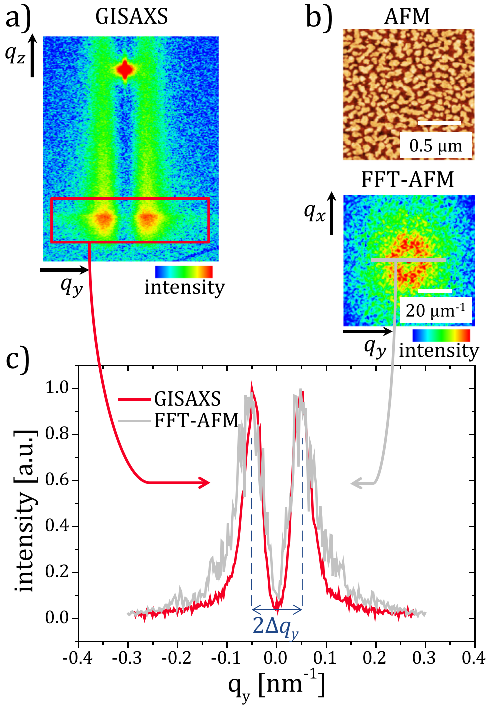

FIG. 4. Determination of the mean island distance $L = 2\pi/\Delta q_y$ of a 0.5 ML thick PTCDI-C_8 film deposited at 70 °C from independent GISAXS (a) and AFM measurements (b). The integrated intensity (along q_z) in the GISAXS region of interest (red rectangle) is plotted as a red line in (c). The characteristic real-space length scales of the AFM image (b) appear as rings in the reciprocal space of the FFT-AFM image. A line scan through the ring yields the gray intensity distribution curve in (c). Good agreement of GISAXS and FFT-AFM intensity distributions is achieved (c), showing approximately the same peak spacing $2\Delta q_y$ and hence the same mean island distance L.

0.5 ML PTCDI-C_8 film in the scattering geometry of Fig. 1(b) during the growth at a substrate temperature of 70 °C and a growth rate of 0.1 nm/min. We observe two separated bright spots in the GISAXS measurement shown in Fig. 4(a). After vertically line-integrating the GISAXS signal in the region of interest (red rectangle), we obtain an intensity distribution in the reciprocal space as shown by the red curve in Fig. 4(c). The spacing $2\Delta q_y$ is inversely proportional to the mean island distance L, with $L = 2\pi/\Delta q_y$.[37] According to our simulations with the GISAXS software BornAgain 1.3.0,[38] the peak spacing is predominantly determined by the mean island spacing, while the influence of the island size and form is insignificant for the peak position.

To demonstrate the equivalence of the GISAXS analysis with the established AFM methods for determining the island density, we directly compare both techniques. An example is given in Fig. 4(b), where we show an AFM image of a 0.5 ML PTCDI-C_8 film deposited at 70 °C and the corresponding 2d fast Fourier transformation (FFT) of this image. A line scan through the center of the so-called Henzler ring[8,10,39] results in an intensity distribution in the reciprocal space. In equivalence to the GISAXS measurement, the peak spacing $2\Delta q_y$ is related to the mean island distance $L = 2\pi/\Delta q_y$. As shown in the example of our datasets in Fig. 4(c), the GISAXS (red) and FFT-AFM (grey) curves agree well indicating the same mean island distance L.

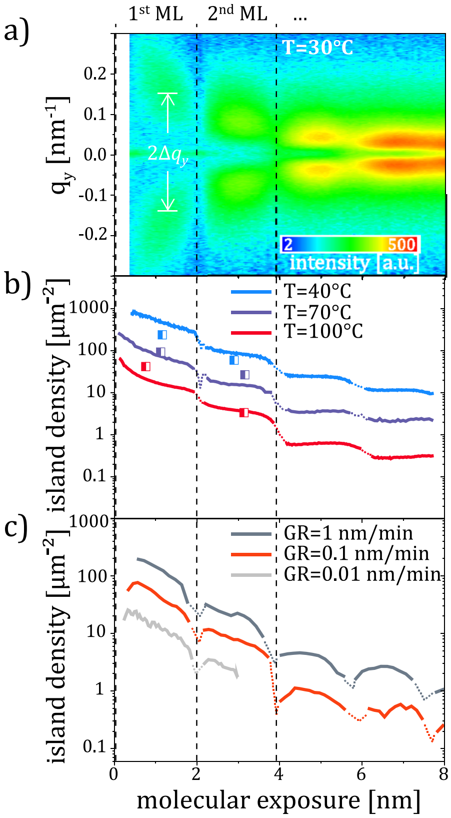

FIG. 5. (a) Time evolution of the diffuse scattering (GISAXS) during the PTCDI-C_8 growth at a substrate temperature of $T = 30$ °C and a growth rate of $GR = 0.1$ nm/min. Two separate peaks, whose intensity oscillates with a period of 1 ML, are observed. The peak spacing is related to the mean island distance L *via* $L = 2\pi/\Delta q_y$ and, therefore, to the island density. From GISAXS datasets similar to (a) the evolution of the island density is obtained for (b) different temperatures and constant $GR = 0.1$ nm/min and (c) different growth rates at constant $T = 80$ °C. The island density can be tuned by about 2 orders of magnitude *via* the substrate temperature and growth rate. The half-filled squares in (b) correspond to island densities obtained from FFT transformed AFM images as discussed in the main text.

The high brilliance of the MiNaXS beamline and the dynamic range of the PILATUS 300K detector enable us to acquire 10-15 frames/ML similar to the one shown in Fig. 4(a) during the growth of PTCDI-C_8. Technically even higher time resolutions are possible, but we set this artificial limit to avoid beam damage. An example of the time evolution of the GISAXS intensity distribution is displayed in Fig. 5(a). For a bare substrate or for a smooth, closed ML essentially no GISAXS signal is acquired. However with the emergence of islands, the GISAXS intensity increases. Subsequently the islands grow laterally and coalesce, so that the mean island distance $L = 2\pi/\Delta q_y$ increases. We, thus, observe that both the intensity and the peak spacing oscillate with a period of 1 ML.

By using $N = \frac{2}{\sqrt{3}} \cdot \frac{1}{L^2}$ we can calculate the island density N from the GISAXS peak spacing assuming an approximately hexagonal packing. The so obtained island density as a function of the molecular exposure is plotted in Fig. 5(b) for a variation of the substrate temperature ($GR = 0.1$ nm/min) and in Fig. 5(c) for a variation of GR ($T = 80$ °C). Note that the island density of PTCDI-C_8 can be tuned by around two orders of magnitude *via* increasing the substrate temperature by 60 °C. The values of N in the beginning or end of a ML growth are deduced from weak scattering signals of very small islands (or holes in the film). Therefore the accuracy can be influenced by other weak scattering contributions around $q_y = 0$ nm^{-1} originating from the substrate, as well as weak GISAXS intensity due to the small roughness of a lower lying complete ML. We indicated the corresponding regions in Figs. 5(b) and 5(c) as dashed lines as a guide to the eye.

For comparison, the island densities from FFT-AFM images are plotted as half-filled squares in Fig. 5(b). Qualitatively a good agreement of both datasets is achieved with the island densities deduced from FFT-AFM showing the same trend of larger islands at higher temperatures and in the higher MLs. Quantitatively the values obtained by the two different methods deviate on average by about 50%. One of the reasons for such deviations is a different statistical average. GISAXS samples an X-ray footprint of 10 mm × 30 µm and provides thus a better statistical average compared to the AFM, where the image size is in the range of 100 µm^2. As a result, fluctuations in the AFM are observed from image to image. This statistical error may be estimated to be in the order of $\sqrt{N \cdot \text{area}}$. Another aspect, which should be taken into account when analyzing the deviations of the island densities, is the dependency of N on the mean island distance L. Due to $N \propto {}^1/_{L^2}$ even small differences in the determination of L by AFM and GISAXS are more pronounced in N, since L enters quadratically. Furthermore the deviations in N may also result from post-growth transformations of the film morphology. While with GISAXS we probe the film *in situ*, the AFM images are taken *ex situ*. As a result, the contact with ambient air, but also effects like wetting or partial desorption may influence the morphology and, thus, may affect the island density measured by AFM. Finally, we emphasize that at the moment few studies are published, which quantitatively compare GISAXS and AFM data for small organic molecules at a comparable level of detail.

We will now analyze the obtained experimental results on the growth of the first MLs of PTCDI-C$_8$ in the framework of mean field nucleation theory, which will allow us to determine important quantities like the nucleation energy and the critical nucleus size. In the 1980s, Venables *et al.* summarized a mathematical model for the description of nucleation and growth phenomena.[6] A central result of their work is a power-law that connects the maximum island density N_{max} with the growth rate GR and the substrate temperature T as given in Ref. 40,

$$N_{max} = \eta \cdot N_0 \cdot \left(\frac{4 \cdot GR}{N_0 \cdot \nu_0}\right)^p \cdot \exp(E_{nuc}/kT). \qquad (1)$$

The exponent p is a function of the critical nucleus size i, which is defined as the number of monomers required to form the largest non-stable cluster. Islands containing $i + 1$ monomers are hence more likely to stay stable than to decay. The nucleation energy E_{nuc} contains a dependency on i as well as on various energy barriers for different molecular processes. The pre-factor η is a weakly varying function of the coverage and i being typically 0.2-0.3,[6] while ν_0 is the attempt frequency for surface diffusion. The number of surface sites per unit area, N_0, equals $2.27 \cdot 10^{14}$ molecules/cm^2 in the PTCDI-C$_8$ [001] plane based on the thin-film unit cell parameters by Krauss *et al.*[20] Various publications have implemented Equation (1) to describe nucleation and growth of both organic and inorganic materials.[40–43]

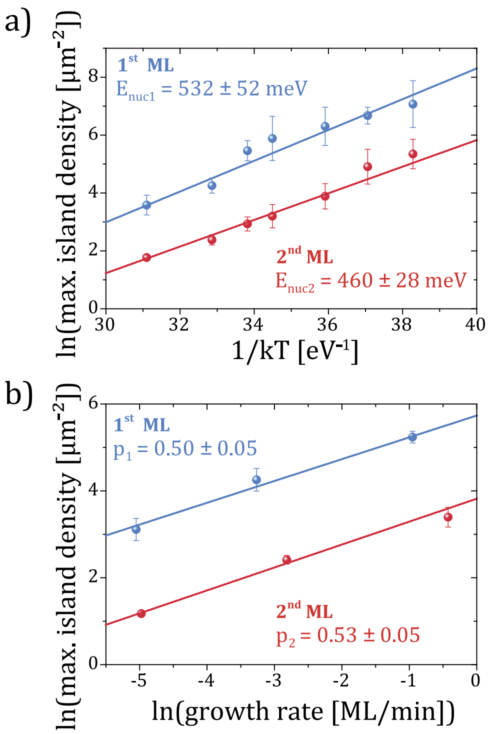

FIG. 6. (a) Determination of the nucleation energy in the 1st and 2nd ML on the basis of the maximum island densities obtained from GISAXS data. A decrease of the nucleation energy is observed in the 2nd ML. (b) Illustration of the linear behavior of the logarithm of the maximum island density as obtained by GISAXS in the 1st and 2nd ML under a variation of the effective ML growth rate (as obtained from the anti-Bragg fits). The slope p, which is related to the critical nucleus size, essentially does not change within the first two MLs.

To evaluate and compare p and E_{nuc} in both MLs we plot the logarithm of the maximum island density as obtained from GISAXS in a $\ln(N_{max})$ vs. $\ln(GR)$ and a $\ln(N_{max})$ vs. $1/kT$ plot as shown in Figs. 6(a) and 6(b). According to Equation (1), we expect a linear relationship in each case with the slopes being p and E_{nuc}, respectively. Note that we use the effective growth rates of the 1st and 2nd ML as deduced from the anti-Bragg fits for the plot of Fig. 6(b), so that we correct for the slower growth in the first ML. As demonstrated, we obtain the predicted linear relation for the nucleation of 1st and 2nd PTCDI-C$_8$ ML, which points towards homogenous nucleation for both MLs. The fits yield values of $E_{nuc1} = 532 \pm 52$ meV and $p_1 = 0.50 \pm 0.05$ for the 1st ML and $E_{nuc2} = 460 \pm 28$ meV and $p_2 = 0.53 \pm 0.05$ for the 2nd ML. Importantly, we find that the nucleation energy E_{nuc} is about 70 meV smaller in the 2nd ML while the parameter p is essentially identical within the error bars in both MLs. We will use these findings later to discuss the diffusivity of the molecules.

Additionally to E_{nuc} and p we can also determine the attempt frequency for surface diffusion υ_0 from the linear fits shown in Figs. 6(a) and 6(b). To do so, we evaluate the intersections of the linear curves with the y-axis, which are given as

$$\begin{aligned} y_{0R} &= \ln(\eta\cdot N_0) + p\cdot\ln\left(\frac{4}{\upsilon_0\cdot N_0}\right) + E_{nuc}\cdot\frac{1}{kT},\\ y_{0T} &= \ln(\eta\cdot N_0) + p\cdot\ln\left(\frac{4}{\upsilon_0\cdot N_0}\right) + p\cdot\ln(GR), \end{aligned} \tag{2}$$

with y_{0R} and y_{0T} being the intercepts of the linear fits in the $\ln(N_{max})$ vs. $\ln(GR)$ and $\ln(N_{max})$ vs. $1/kT$ plots, respectively. By inserting p and E_{nuc} we calculate the attempt frequency for surface diffusion ν_0 in both MLs, since all the other quantities are known. Importantly, essentially the same frequencies are deduced from the fits to the temperature and rate variation, which proves the consistency of the model and the data. We derive attempt frequencies for surface diffusion of $\nu_{0,1} \approx 10^{20\pm3}$ s^{-1} in the 1st ML and $\nu_{0,2} \approx 10^{19\pm3}$ s^{-1} in the 2nd ML. Note that small changes in p induce comparatively large changes in ν_0. Thus, within the errors introduced by the uncertainty in p, $\upsilon_{0,1}$ and $\upsilon_{0,2}$ may be assumed to equal. In comparison to that, for atomic systems typical attempt frequencies for surface diffusion in the range of 10^{13} s^{-1} are reported. For small organic molecules, however, few published data are available. In one study, an attempt frequency for surface diffusion of 10^{17} s^{-1} has been found for the organic molecule sexiphenyl on amorphous mica.[40] As reported in Ref. 40, due to the increased number of rotational and vibrational modes that can be excited in organic molecules in comparison to atomic systems, larger attempt frequencies for surface diffusion are expected. Our findings confirm this trend.

IV. DISCUSSION

In what follows, we will compare the PTCDI-C$_8$ nucleation in the 1st and 2nd ML in order to rationalize the observed decrease of the island density in the 2nd ML by quantifying the differences in the molecular diffusivity. For this purpose we will combine the evaluated values of p, E_{nuc}, and ν_0 of both MLs. Depending on the examined parameter space of T and GR, different energetic barriers may govern the nucleation, so that various nucleation regimes can be formulated which are summarized in Fig. 7(b).

A fundamental difference between the regimes is whether they describe complete or incomplete condensation. If a significant fraction of already adsorbed molecules desorbs from the surface before attaching to a cluster, the condensation is regarded as incomplete. Such behavior was, e.g., observed by Ribič *et al.*[43] for pentacene films grown on polymeric substrates at substrate temperatures above 50 °C. The authors observed a shrinking monolayer growth rate by approximately 35% per 10 °C increase in the substrate temperature and applied the initially incomplete condensation (IIC) model for fitting. In contrast, in the case of PTCDI-C$_8$ the fits of the anti-Bragg growth oscillations show the same effective GR for the growth at 40 °C and 100 °C. Thus, we conclude that molecular desorption is not the dominating process in the investigated parameter range and the condensation can be regarded as complete. Crucially, complete condensation does not imply that every incoming molecule will actually be adsorbed and will stick to the surface. Different sticking coefficients may thus explain our finding of different effective 1st and 2nd ML growth rates.

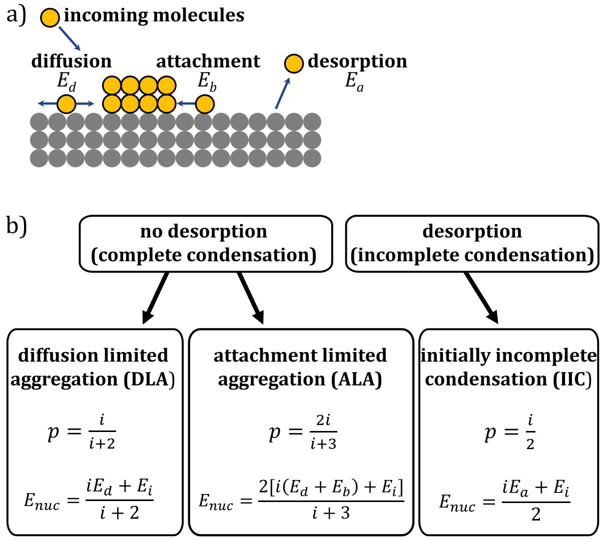

FIG. 7. (a) Illustration of relevant molecular processes and energy barriers involved in organic thin-film growth. (b) Summary of the exponents p and E_{nuc} from Equation (1) as defined for two different nucleation regimes. Depending on the particular regime, diffusion energy E_d, binding energy of a critical nucleus E_i, the attachment barrier E_b, and desorption energy E_a can contribute to the effective nucleation energy E_{nuc}. The scaling exponent p is always a function of the critical nucleus size i.

For the case of complete condensation, the most frequently used nucleation regime is diffusion limited aggregation (DLA) with $p = i/(i+2)$ and $E_{nuc} = (iE_d + E_i)/(i+2)$. The binding energy of a critical nucleus E_i is included in E_{nuc}. However since in complete condensation a detachment of already adsorbed molecules from the surface is zero or insignificant, the nucleation energy does not depend on the desorption energy E_a, but on the energy barrier for diffusion E_d.

By applying DLA and using the determined quantities of p and E_{nuc}, one can evaluate the critical nucleus size and discuss the evolution of the energy barrier for surface diffusion E_d in the 1st and 2nd ML. As shown in Fig. 6(b), the exponential factor p is similar in both MLs. According to the definition of p in the DLA regime, this implies that the critical nucleus size also has to be equal in both MLs and it has to be $i = 2$ if inserting the values of p_1 and p_2. To our knowledge, no data on the size of critical PTCDI-C$_8$ clusters are available in the literature. Looking at the critical cluster sizes of other rod-like molecules, values of i = 2-3 for *para*-sexiphenyl,[40,44] $i = 5 \pm 2$ for pentacene,[45–48] and $i = 2$ of diindenoperylene[47] have been published. Interestingly, for the related, but heavier PTCDI-C$_{13}$ molecule grown on various organic self-assembled monolayers, a cluster size of $i = 1$ was reported recently.[31] We note, however, i is known to depend on exact growth parameters such as the substrate temperature.[49,50]

Further, to evaluate E_d we use the definition of $E_{nuc} = (iE_d + E_i)/(i+2)$ as given in the DLA model and insert this in the relation $E_{nuc1} - E_{nuc2} = 70$ meV as determined from Fig. 6(a). Since the critical nucleus size is identical ($i = 2$), the binding energy of the critical nucleus E_i has also to be equal $E_{i,1} = E_{i,2} = E_i$ in both MLs. Combining this we find

$$E_{d1} - E_{d2} = 140\ \text{meV}. \tag{3}$$

The result of Equation (3) is that the energetic barrier for diffusion in the 2nd ML is 140 meV lower. This indicates a higher diffusivity D in the 2nd ML, but according to the definition of $D = \nu_0 \cdot \exp(-E_d/kT)$ the attempt frequency for surface diffusion also plays an important role. A decreased attempt frequency in the 2nd ML may outbalance the effect of a decreased diffusion barrier. This is, however, not the case for PTCDI-C$_8$. Although we found a slightly decreased υ_0 in the 2nd ML ($\nu_{0,2} = 0.1 \cdot \nu_{0,1}$), comparing the diffusivities in both MLs, there is still an increased molecular mobility in the 2nd ML accounting for the decreased island density in the evaluated T range,

$$\begin{aligned} D_2 &= D_1 \cdot \left[\frac{\nu_{0,2}}{\nu_{0,1}} \cdot \exp\left(\frac{-(E_{d2} - E_{d1})}{kT}\right)\right] \\ &\approx (25 \ldots 250) \cdot D_1|_{T=293\text{K}}. \end{aligned} \tag{4}$$

Assuming $\nu_{0,1} \approx 10^{20}\ \text{s}^{-1}$ and $\nu_{0,2} \approx 10^{19}\ \text{s}^{-1}$ we find a 25 times larger diffusivity in the 2nd ML, while the assumption of the same ν_0 in both MLs yields a 250 times increased diffusivity at room temperature. In the literature, decreased island densities in the 2nd ML have been reported, e.g., for diindenoperylene on silicon oxide.[12] The study also found a decrease of E_{nuc} in the 2nd ML of 100 meV, which is comparable in size with the present case of PTCDI-C$_8$. However, neither E_d and ν_0 nor the diffusivity have been evaluated directly. The effect of a decreasing diffusion barrier and decreasing island densities in higher MLs has however been found for the case of inorganic Co films grown of Fe(001).[51]

While in the past most nucleation studies of organic molecules have been relying on the DLA model, over the last years this model has been refined by taking additional and new effects into account, in particular so-called attachment barriers[27] (ALA regime) and hot precursor states.[28,52] Contrary to DLA, in the case of the ALA regime the probability of a molecule to attach to a molecular island is different than unity and the molecule has to overcome the attachment barrier energy E_b. E_b can be regarded as the energy needed to reorient the molecule from the flat lying state when freely diffusing to an almost upright standing state when attaching to an island.[27,53] In the case of ALA, E_b enters E_{nuc} and furthermore the definition of p changes as summarized in Fig. 7(b). Applying ALA in both MLs for the case of PTCDI-C$_8$, one finds a critical nucleus size of $i = 1$, since $p_1 \approx p_2 \approx 0.5$. One can additionally use the ALA definition of E_{nuc} and $E_{nuc1} - E_{nuc2} = 70$ meV from Fig. 6(a) in order to arrive at the following equation:

$$(E_{d1} + E_{b1}) - (E_{d2} + E_{b2}) = 140\ \text{meV}. \tag{5}$$

Since the nucleation is homogeneous, the attachment barrier E_b originates from a direct in-plane interaction of the organic molecules. Consequently, one can expect a small dependence of E_b on the underlying layer. As a result of this assumption $E_{b1} \approx E_{b2}$, Equation (5) transforms into Equation (3), with the same consequences concerning the increased molecular diffusivity in the 2nd ML.

A third model, that has recently been applied in the context of organic nucleation, includes so-called hot precursor states.[28,52] Commonly, hot molecules from the crucible, which impinge on a surface are assumed to transfer their whole kinetic energy to the substrate material and adopt its temperature. However if this thermalization process is slow, individual molecules may still possess some additional, remaining kinetic energy, resulting in a higher diffusivity than expected for a given substrate temperature. The effective temperature T_{eff} of the molecules can then be denoted as $T_{eff} = T_i - \kappa \cdot (T_i - T_s)$, with T_i being the temperature of evaporation, T_s the substrate temperature, and κ the so-called energy dissipation coefficient. According to Ref. 28 in the case of hot precursor states, the maximum island density can be described as follows:

$$\begin{aligned} N_{max} = 10^{-8} \cdot N_0 \cdot \left(\frac{4 \cdot GR}{N_0 \cdot \nu_0}\right)^p \\ \cdot \exp(E_{nuc}/k \cdot (T_i - \kappa \cdot (T_i - T_s))). \end{aligned} \tag{6}$$

As given by the ALA model $p = 2i/(i+3)$ and $E_{nuc} = 2[i(E_d + E_b) + E_i]/(i+3)$. Equation (6) can in principle be applied to fit the datasets of $\ln(N_{max})$ vs. T_s and $\ln(N_{max})$ vs. $\ln(GR)$, although the fit is clearly overparameterized with υ_0, E_{nuc} and κ being unknown (the exponent p is still the slope in the $\ln(N_{max})$ vs. $\ln(GR)$ plot in equivalence to the DLA/ALA model). However, one can investigate E_{nuc} and κ in both MLs by assuming various υ_0. Independent of the chosen υ_0, we observe the following trend. The fits show a decreasing E_{nuc} by about 70-80 meV in the 2nd ML, which is similar to the results from DLA/ALA. In parallel, the energy dissipation coefficient κ is slightly increasing (see the supplementary material[51] and Fig. S1 for the fits), although the overparameterized model does not allow for a unique fit of κ. A higher κ points towards a decreased effective temperature of the molecules in the higher ML in which the impinging molecules hit material of the same mass. The soft organic monolayer absorbs more of the initial kinetic energy than the hard silicon surface. The difference in the energy dissipation may hence also influence the nucleation and growth behavior in different MLs, which is a new and yet largely unstudied phenomenon.

V. CONCLUSIONS

We have examined the ML-dependent nucleation and growth of the organic semiconductor PTCDI-C$_8$ deposited on silicon oxide substrates. For our study we combined *ex situ* AFM and *in situ* real-time X-ray scattering, where we simultaneously monitored the temporal evolution of the in-plane (GISAXS) and the out-of-plane (XRR) thin-film morphology in individual MLs beyond submonolayer nucleation.

We identified important differences in the nucleation and growth behavior of the 1st and the subsequent MLs of PTCDI-C$_8$, such as a transformation of the island shapes, as well as an increase of the molecular adsorption probabilities. Of particular interest is the observed decrease of the molecular island density in higher layers. Such a trend indicates an enhancement of molecular diffusivity. To verify this, we examined the scaling of the maximum island densities N_{max} in each individual ML as a function of the substrate temperature and the growth rate. We fitted the observed N_{max} scaling by applying classical diffusion-limited aggregation (DLA) as well as more recent models such as attachment-limited aggregation (ALA) within the mean-field nucleation theory. From the models, we determined the same critical nucleus size i in both MLs ($i = 2$ in DLA and $i = 1$ in ALA) and a slight decrease of the attempt frequency for surface diffusion ν_0. Furthermore we determined a 70 meV decrease of the nucleation energy E_{nuc} in the 2nd ML. Combining the data we evaluated a significant decrease of 140 meV of the energy barrier for diffusion E_d, which correlates with an at least 25 times larger molecular diffusivity in the 2nd ML at room temperature. This finding explains the observation of a decreased island density in upper MLs. Applying a hot precursor model hints additionally at a different thermalization in the 2nd ML as compared to the 1st ML.

Compared to inorganic material systems, the nucleation and growth of organic molecules is more intricate due to the complexity of the molecular shapes that influence the self-assembly. One of the most challenging tasks remains the determination of energetic barriers and nanoscale processes like molecular diffusion. Our approach of expanding the analysis of organic semiconductor nucleation beyond the first (sub-) monolayer regime to subsequent MLs allows us to identify and quantify important changes of structure defining processes as demanded for an enhanced comprehension of the thin-film formation.

SUPPLEMENTARY MATERIAL

See supplementary material for fits of the maximum island density on the basis of the hot precursor model.

ACKNOWLEDGMENTS

We are grateful for the provided beamtime at the P03 beamline of the light source PETRAIII at DESY – a member of the Helmholtz Association (HGF). We thank S. V. Roth for help during the synchrotron experiments. The authors acknowledge the support of E. Merzlyakova with data analysis and M. Gensler with AFM image acquisition. We acknowledge financial support of the DFG within the CRC 951 – Hybrid Inorganic/Organic Systems for Opto-Electronics (HIOS).

[1] S. Tasch, C. Brandstätter, F. Meghdadi, G. Leising, G. Froyer, and L. Athouel, Adv. Mater. **9**, 33 (1997).
[2] C. Simbrunner, G. Hernandez-Sosa, E. Baumgartner, G. Hesser, J. Roither, W. Heiss, and H. Sitter, Appl. Phys. Lett. **94**, 073505 (2009).
[3] H. T. Yi, M. M. Payne, J. E. Anthony, and V. Podzorov, Nat. Commun. **3**, 1259 (2012).
[4] B. Schmidt-Hansberg, M. Sanyal, M. F. G. Klein, M. Pfaff, N. Schnabel, S. Jaiser, A. Vorobiev, E. Müller, A. Colsmann, P. Scharfer, D. Gerthsen, U. Lemmer, E. Barrena, and W. Schabel, ACS Nano **5**, 8579 (2011).
[5] Z. Li, H. C. Wong, Z. Huang, H. Zhong, C. H. Tan, W. C. Tsoi, J. S. Kim, J. R. Durrant, and J. T. Cabral, Nat. Commun. **4**, 2227 (2013).
[6] J. A. Venables, G. D. T. Spiller, and M. Hanbucken, Rep. Prog. Phys. **47**, 399 (1984).
[7] H. Brune, Surf. Sci. Rep. **31**, 125 (1998).
[8] J. W. Evans, P. A. Thiel, and M. C. Bartelt, Surf. Sci. Rep. **61**, 1 (2006).
[9] G. Renaud, R. Lazzari, C. Revenant, A. Barbier, M. Noblet, O. Ulrich, F. Leroy, J. Jupille, Y. Borensztein, C. R. Henry, J.-P. Deville, F. Scheurer, J. Mane-Mane, and O. Fruchart, Science **300**, 1416 (2003).
[10] J. D. Ferguson, G. Arikan, D. S. Dale, A. R. Woll, and J. D. Brock, Phys. Rev. Lett. **103**, 256103 (2009).
[11] S. Bommel, N. Kleppmann, C. Weber, H. Spranger, P. Schäfer, J. Novak, S. V. Roth, F. Schreiber, S. H. L. Klapp, and S. Kowarik, Nat. Commun. **5**, 5388 (2014).
[12] C. Frank, J. Novák, R. Banerjee, A. Gerlach, F. Schreiber, A. Vorobiev, and S. Kowarik, Phys. Rev. B **90**, 045410 (2014).
[13] M. Ruge, F. Golks, J. Zegenhagen, O. M. Magnussen, and J. Stettner, Phys. Rev. Lett. **112**, 055503 (2014).
[14] B. Krause, F. Schreiber, H. Dosch, A. Pimpinelli, and O. H. Seeck, Europhys. Lett. **65**, 372 (2004).
[15] A. C. Mayer, R. Ruiz, H. Zhou, R. L. Headrick, A. Kazimirov, and G. G. Malliaras, Phys. Rev. B **73**, 205307 (2006).
[16] S. Kowarik, A. Gerlach, S. Sellner, F. Schreiber, L. Cavalcanti, and O. Konovalov, Phys. Rev. Lett. **96**, 125504 (2006).
[17] A. Amassian, T. V. Desai, S. Kowarik, S. Hong, A. R. Woll, G. G. Malliaras, F. Schreiber, and J. R. Engstrom, J. Chem. Phys. **130**, 124701 (2009).
[18] S. Kowarik, A. Gerlach, M. W. A. Skoda, S. Sellner, and F. Schreiber, Eur. Phys. J.: Spec. Top. **167**, 11 (2009).
[19] S. Y. An, K. Ahn, D. Y. Kim, H.-H. Lee, J. H. Cho, and D. R. Lee, J. Chem. Phys. **140**, 154702 (2014).
[20] T. N. Krauss, E. Barrena, X. N. Zhang, D. G. de Oteyza, J. Major, V. Dehm, F. Würthner, L. P. Cavalcanti, and H. Dosch, Langmuir **24**, 12742 (2008).
[21] T. N. Krauss, E. Barrena, D. G. de Oteyza, X. N. Zhang, V. Dehm, F. Wu, and H. Dosch, J. Phys. Chem. C **113**, 4502 (2009).
[22] P. R. L. Malenfant, C. D. Dimitrakopoulos, J. D. Gelorme, L. L. Kosbar, T. O. Graham, A. Curioni, and W. Andreoni, Appl. Phys. Lett. **80**, 2517 (2002).
[23] R. J. Chesterfield, J. C. McKeen, C. R. Newman, P. C. Ewbank, D. A. da Silva Filho, J. L. Brédas, L. L. Miller, K. R. Mann, and C. D. Frisbie, J. Phys. Chem. B **108**, 19281 (2004).
[24] A. L. Briseno, S. C. B. Mannsfeld, C. Reese, J. M. Hancock, Y. Xiong, S. A. Jenekhe, Z. Bao, and Y. Xia, Nano Lett. **7**, 2847 (2007).
[25] S. Karak, V. S. Reddy, S. K. Ray, and A. Dhar, Org. Electron. **10**, 1006 (2009).
[26] E. R. Kish, R. K. Nahm, A. R. Woll, and J. R. Engstrom, J. Phys. Chem. C **120**, 6165 (2016).
[27] L. Tumbek and A. Winkler, Surf. Sci. **606**, L55 (2012).
[28] A. Winkler and L. Tumbek, J. Phys. Chem. Lett. **4**, 4080 (2013).
[29] A. Buffet, A. Rothkirch, R. Döhrmann, V. Körstgens, M. M. Abul Kashem, J. Perlich, G. Herzog, M. Schwartzkopf, R. Gehrke, P. Müller-Buschbaum, and S. V. Roth, J. Synchrotron Radiat. **19**, 647 (2012).
[30] G. Santoro, A. Buffet, R. Döhrmann, S. Yu, V. Körstgens, P. Müller-Buschbaum, U. Gedde, M. Hedenqvist, and S. V. Roth, Rev. Sci. Instrum. **85**, 043901 (2014).
[31] T. V. Desai, E. R. Kish, A. R. Woll, and J. R. Engstrom, J. Phys. Chem. C **115**, 18221 (2011).
[32] T. V. Desai, A. R. Woll, F. Schreiber, and J. R. Engstrom, J. Phys. Chem. C **114**, 20120 (2010).
[33] M. Sparenberg, A. Zykov, P. Beyer, L. Pithan, C. Weber, Y. Garmshausen, F. Carlà, S. Hecht, S. Blumstengel, F. Henneberger, and S. Kowarik, Phys. Chem. Chem. Phys. **16**, 26084 (2014).
[34] P. Beyer, T. Breuer, S. Ndiaye, A. Zykov, A. Viertel, M. Gensler, J. P. Rabe, S. Hecht, G. Witte, and S. Kowarik, ACS Appl. Mater. Interfaces **6**, 21484 (2014).
[35] V. I. Trofimov and V. G. Mokerov, Thin Solid Films **428**, 66 (2003).
[36] A. R. Woll, T. V. Desai, and J. R. Engstrom, Phys. Rev. B **84**, 075479 (2011).
[37] M. Schwartzkopf, A. Buffet, V. Körstgens, E. Metwalli, K. Schlage, G. Benecke, J. Perlich, M. Rawolle, A. Rothkirch, B. Heidmann, G. Herzog, P. Müller-Buschbaum, R. Röhlsberger, R. Gehrke, N. Stribeck, and S. V. Roth, Nanoscale **5**, 5053 (2013).
[38] C. Durniak, M. Ganeva, G. Pospelov, W. van Herck, and J. Wuttke, http://www.bornagainproject.org, 2015.
[39] P. Hahn, J. Clabes, and M. Henzler, J. Appl. Phys. **51**, 2079 (1980).
[40] T. Potocar, S. Lorbek, D. Nabok, Q. Shen, L. Tumbek, G. Hlawacek, P. Puschnig, C. Ambrosch-Draxl, C. Teichert, and A. Winkler, Phys. Rev. B **83**, 075423 (2011).
[41] S. Pratontep, M. Brinkmann, F. Nüesch, and L. Zuppiroli, Phys. Rev. B **69**, 165201 (2004).
[42] J. Yang, T. Wang, H. Wang, F. Zhu, G. Li, and D. Yan, J. Phys. Chem. B **112**, 7816 (2008).
[43] P. R. Ribič, V. Kalihari, C. D. Frisbie, and G. Bratina, Phys. Rev. B **80**, 115307 (2009).

[44] S. Lorbek, G. Hlawacek, and C. Teichert, Eur. Phys. J.: Appl. Phys. **55**, 23902 (2011).

[45] A. S. Killampalli, T. W. Schroeder, and J. R. Engstrom, Appl. Phys. Lett. **87**, 033110 (2005).

[46] B. Stadlober, U. Haas, H. Maresch, and A. Haase, Phys. Rev. B **74**, 165302 (2006).

[47] E. R. Kish, T. V. Desai, D. R. Greer, A. R. Woll, and J. R. Engstrom, J. Vac. Sci. Technol. A **33**, 031511 (2015).

[48] R. Ruiz, B. Nickel, N. Koch, L. C. Feldman, R. F. Haglund, A. Kahn, F. Family, and G. Scoles, Phys. Rev. Lett. **91**, 136102 (2003).

[49] M. Campione, S. Caprioli, M. Moret, and A. Sassella, J. Phys. Chem. C **111**, 12741 (2007).

[50] H. Brune, G. S. Bales, J. Jacobsen, C. Boragno, and K. Kern, Phys. Rev. B **60**, 5991 (1999).

[51] A. Picone, M. Riva, G. Fratesi, A. Brambilla, G. Bussetti, M. Finazzi, L. Duò, and F. Ciccacci, Phys. Rev. Lett. **113**, 046102 (2014).

[52] J. R. Morales-Cifuentes, T. L. Einstein, and A. Pimpinelli, Phys. Rev. Lett. **113**, 246101 (2014).

[53] A. Winkler, Surf. Sci. **652**, 367 (2016).